Volume 17 | Number 12 | 28 March 2015 | Pages 2435–2592

CrystEngComm

www.rsc.org/crystengcomm

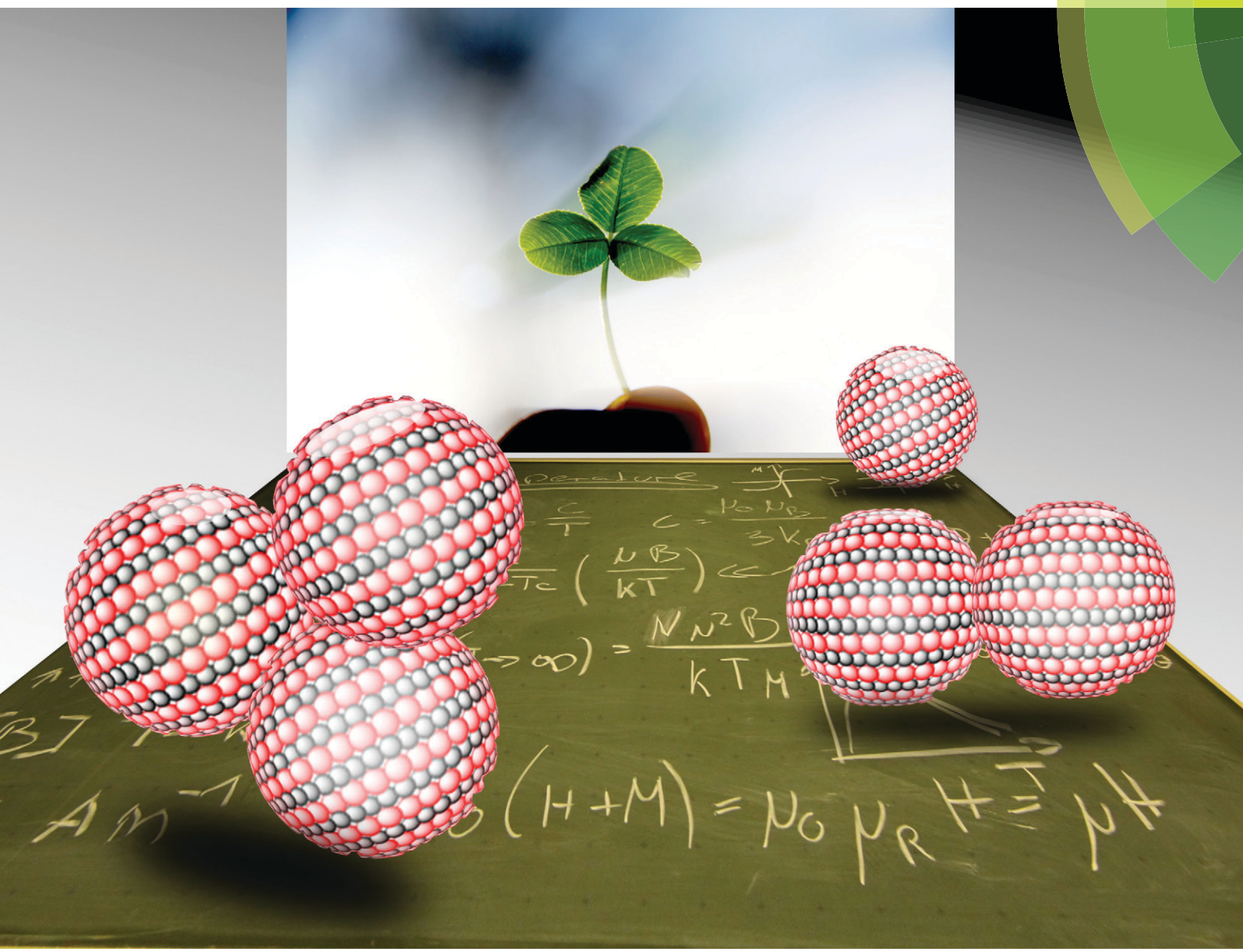

ROYAL SOCIETY OF CHEMISTRY

PAPER

G. Garnweitner *et al.*

Oriented attachment of ultra-small $Mn_{(1-x)}Zn_xFe_2O_4$ nanoparticles during the non-aqueous sol–gel synthesis

CrystEngComm

PAPER

View Article Online
View Journal | View Issue

Open Access Article. Published on 04 December 2014. Downloaded on 12/6/2025 6:08:32 AM.
This article is licensed under a Creative Commons Attribution-NonCommercial 3.0 Unported Licence.

Cite this: *CrystEngComm*, 2015, **17**, 2464

Oriented attachment of ultra-small $Mn_{(1-x)}Zn_xFe_2O_4$ nanoparticles during the non-aqueous sol–gel synthesis†

I.-C. Masthoff,[a] A. Gutsche,[b] H. Nirschl[b] and G. Garnweitner*[a]

Received 14th October 2014,
Accepted 4th December 2014

DOI: 10.1039/c4ce02068e

www.rsc.org/crystengcomm

The advantages of ultra-small manganese–zinc ferrite nanoparticles are manifold and can be exploited in a wide range of applications. Here we show that ultra-small, highly crystalline Mn–Zn ferrite nanoparticles with variable compositions can be obtained by non-aqueous sol–gel synthesis in a facile, scalable process. The growth of $Mn_{0.6}Zn_{0.4}Fe_2O_4$ nanoparticles has been investigated exemplarily for a series of Mn–Zn ferrites. It is thereby shown that the initially formed ultra-small 2 nm sized particles grow *via* oriented attachment into shamrock-like shaped particles, and clusters with an ordered structure are formed during synthesis. Throughout the synthesis, the crystallinity of the particles improves until after 24 h of synthesis highly crystalline, monodisperse nanostructures with a size of around 6 nm are obtained. Furthermore, the influence of the chemical as well as physical properties of the ultra-small $Mn_{(1-x)}Zn_xFe_2O_4$ nanoparticles with $0 \leq x \leq 1$ on their Curie temperature was evaluated. It is shown that by variation of the Mn/Zn ratio the Curie temperature of the particles can be tailored in a broad range from 200 to 400 °C.

1. Introduction

Manganese–zinc ferrite nanoparticles of the general composition $Mn_{(1-x)}Zn_xFe_2O_4$ have been widely investigated for potential use in various electronic applications such as transformers, chock coils, noise filters, *etc.*[1–3] But this spinel ferrite is also highly promising for many applications in biomedicine, some of which are magnetic carriers, bioseparation and protein immobilization.[4–7] Furthermore Mn–Zn ferrite finds industrial applications because of its magnetic permeability, low core loss and adjustable Curie temperature.[8]

The magnetic properties such as the saturation magnetization or the Curie temperature of manganese–zinc ferrites depend strongly on their chemical composition and grain size.[9] In 1960, Verhaeghe *et al.*[10] found that the Curie temperature of $Mn_{(1-x)}Zn_xFe_2O_4$ decreases when the content of Zn is increased, which was confirmed in later studies.[11,12]

Several methods are reported for the synthesis of $Mn_{(1-x)}Zn_xFe_2O_4$ nanoparticles. Conventionally the ceramic process is used to synthesize these ferrites. This preparation route has the disadvantage that very high sintering temperatures (>1300 °C) have to be applied,[13] leading to strong sintering and grain growth that impede the preparation of defined nanoparticles. As an alternative to this process, various other methods have been developed for the preparation on a laboratory scale, such as the microemulsion synthesis,[14] co-precipitation,[15] sol–gel synthesis[16] and hydrothermal synthesis.[17] Many physical and chemical properties of the ferrites depend on the preparation technique and conditions. Thus, new efficient synthesis routes allowing the production of highly defined ferrites have to be found. The synthesis has to meet the demand that ferrites with defined chemical compositions as well as physical properties can be produced in a reproducible fashion.

In this paper, we present the non-aqueous sol–gel synthesis of ultra-small manganese–zinc ferrite nanostructures and show their growth by oriented attachment of individual building blocks. Highly crystalline nanostructures with variable composition and thus variable Curie temperature were obtained with good reproducibility whilst presenting with the possibility of a scale-up. The usage of ultra-small nanoparticles shows advantages in various applications such as for the purification of proteins[18,19] where a large specific surface area offers the benefit of a larger number of binding sites available to bind the target protein. Likewise such small magnetic nanoparticles show great potential as contrast agents used in magnetic resonance imaging (MRI) or molecular imaging due to their longer circulation half-life and better

[a] *Institute for Particle Technology and Laboratory for Emerging Nanometrology, Technische Universität Braunschweig, Braunschweig, Germany.*
E-mail: g.garnweitner@tu-braunschweig.de; Fax: +49 (0)531 3919633; Tel: +49 (0)531 3919615
[b] *Institute for Mechanical Process Engineering and Mechanics, Karlsruhe Institute of Technology, Karlsruhe, Germany*

† Electronic supplementary information (ESI) available. See DOI: 10.1039/c4ce02068e

This journal is © The Royal Society of Chemistry 2015

Open Access Article. Published on 04 December 2014. Downloaded on 12/6/2025 6:08:32 AM.
This article is licensed under a Creative Commons Attribution-NonCommercial 3.0 Unported Licence.

contrast.[20,21] Furthermore the application of ultra-small nanoparticles is preferable for use in thin films as an improved homogeneity can be achieved.[22,23]

2. Experimental

2.1. Synthesis of $Mn_{(1-x)}Zn_xFe_2O_4$

All reagents were of analytical grade obtained from Sigma Aldrich and were used without further purification. $Mn_{(1-x)}Zn_xFe_2O_4$ nanoparticles with $0 \leq x \leq 1$ were synthesized *via* the non-aqueous sol–gel method using dry triethylene glycol as high boiling organic solvent. Iron(III) acetylacetonate, manganese(II) acetylacetonate and zinc acetylacetonate hydrate or zinc acetate were used as precursors. All reagents were dried at 100 °C for 1 h prior to usage. In a typical preparation procedure for $Mn_{0.6}Zn_{0.4}Fe_2O_4$ nanoparticles, 5 mmol of $Fe(acac)_3$, 1.5 mmol of $Mn(acac)_2$ and 1 mmol of $Zn(acac)_2$ were dissolved in 20 ml of triethylene glycol (TEG). The mixture was sealed in a Teflon-lined stainless steel autoclave (45 mL capacity) and heated to 200 °C, which was maintained for 24 h.

For the analysis performed on dried samples, the particles were washed three times by addition of 20 mL of acetone. In the first washing step, the particles were centrifuged at 6900 rpm for 10 minutes to retrieve the particles from the reaction mixture. In the following washing steps, the particles were removed magnetically by attaching a permanent neodymium magnet (cubic shape with 1 cm edge length) to one side of the centrifuge tube. Subsequently the samples were vacuum dried for 24 h at room temperature.

For transmission electron microscopy (TEM) and dynamic light scattering analysis (DLS), the samples were washed likewise and transferred to 10 mL of chloroform, stabilizing them with 30 μL of oleic acid. The excess oleic acid was removed after 24 h by washing the particles twice with acetone followed by dispersing them again in 10 mL of chloroform.

For flame atomic absorption spectroscopy (F-AAS) and inductively coupled plasma-optical emission spectrometry (ICP-OES), the calcinated samples were digested *via* a soda–potash fusion and then dissolved in 5 mL of 6 M HCl.

2.2. Characterization

X-ray diffraction (XRD) was performed on the dried as well as the calcinated samples to analyze the crystallinity and the crystallite size with Cu Kα radiation (Empyrean Cu LEF HR goniometer) on a Si sample holder in a range of 2Θ from 20° to 90° and a step size of 0.05° (Empyrean series 2, PANalytical, PIXcel-3D detector).

Small-angle X-ray scattering (SAXS) measurements of the particles dispersed in TEG were carried out on a SAXSess mc^2 system (Anton Parr) using Cu Kα radiation and a CCD detector, measuring the samples three times for 50 s. The obtained 1D patterns were corrected for transmission and instrument background.

Transmission electron microscopy (TEM) images of the samples were obtained using a FEI TECNAI F30 at 300 kV with 200 mesh holey carbon coated copper grids (Plano GmbH) to specify the particle shape, size and crystallinity.

DLS measurements were performed using a Zetasizer NS, Malvern, carrying out a 173° backscatter measurement with three repeated runs to determine the sizes of the obtained particles.

Flame atomic absorption spectroscopy (F-AAS) (Analytic Jena ZEEnit 700) was used to determine the compositions of the samples. Additionally ICP-OES measurements were carried out on a Vista MPX from Varian using calibration solutions from Specpure, Alfa Aesar.

Thermogravimetric analysis was performed on the calcinated samples to determine the Curie temperature. For the determination of the Curie temperature, the dried particles were initially calcinated at 400 °C for 2 h in a nitrogen atmosphere to ensure that the organic residue on the surface of the particles did not affect the measurement. All TGA measurements were carried out on a Mettler Toledo TGA/SDTA 851 under N_2 in the range of 25–800 °C at 10 °C min^{-1} with a permanent neodymium magnet (136.3 N) placed underneath the sample on the outer TGA furnace wall.

DC-susceptibility measurements were performed using an MPMS-5S from Quantum Design in a liquid cell made from PVC.

3. Results and discussion

X-ray diffraction (XRD) analysis was used to determine the crystallinity and the crystallite size of the nanoparticles. The XRD patterns of the dried samples are shown in Fig. 1. All samples show the typical reflections of the cubic spinel structure, with the characteristic (311) reflection at around 35.0° 2Θ. The patterns are in good agreement with JCPDS card 88-1965 for $MnFe_2O_4$, 74-2402 for $Mn_{0.8}Zn_{0.2}Fe_2O_4$, 74-2401 for $Mn_{0.6}Zn_{0.4}Fe_2O_4$, 74-2400 for $Mn_{0.4}Zn_{0.6}Fe_2O_4$, 74-2399 for $Mn_{0.2}Zn_{0.8}Fe_2O_4$ and 70-3383 for $ZnFe_2O_4$. The reflections of the prepared samples are broadened due to the nanocrystalline nature of the samples. Moreover, for samples where the Zn : Mn ratio is >80% and zinc acetylacetonate hydrate is used as a precursor, two phases are detected (Fig. S1†), one being the spinel ferrite $Mn_{(1-x)}Zn_xFe_2O_4$ and the other being the hexagonal ZnO. Using zinc acetate as a precursor for the compositions with a high zinc content results in the phase pure ferrite. We suppose that this is due to the higher melting point of zinc acetate, at 237 °C instead of 126 °C for zinc acetylacetonate (Fig. 1, bottom).

The samples calcinated at 400 °C for 2 h in a nitrogen atmosphere for the Curie temperature analysis show an increase in crystallinity as indicated by the sharpening of the reflections (Fig. S2†). Further changes of the samples are not noted which can be attributed to their high thermal stability.

The average crystallite size for the particles was calculated from the line width of the (311) reflection using the Scherrer equation. For all samples, except for the $ZnFe_2O_4$ sample, a mean size of around 5 nm was calculated for the dried samples. The $ZnFe_2O_4$ particles are slightly larger with a mean diameter of 8 nm.

Open Access Article. Published on 04 December 2014. Downloaded on 12/6/2025 6:08:32 AM.
This article is licensed under a Creative Commons Attribution-NonCommercial 3.0 Unported Licence.

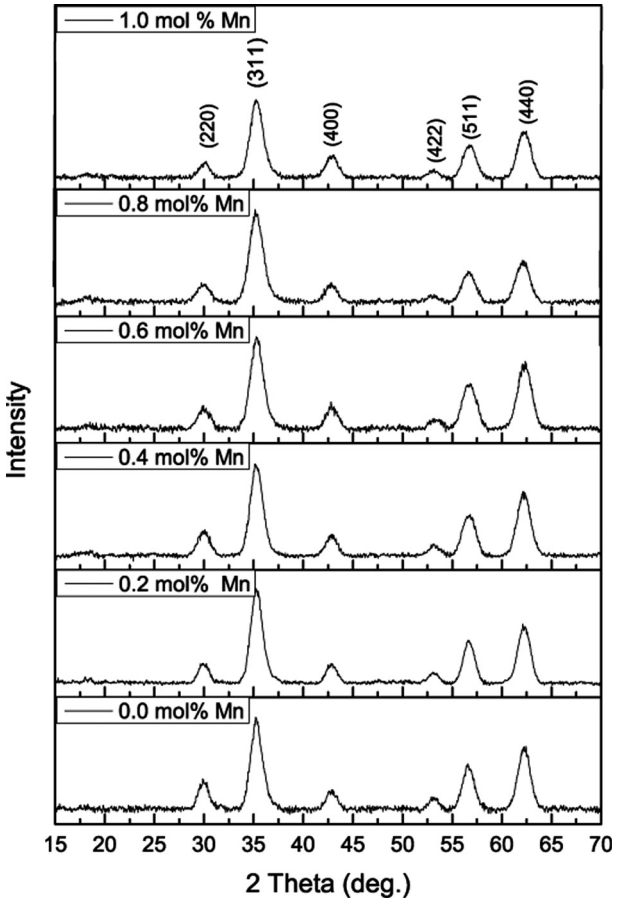

Fig. 1 XRD diffraction patterns of the dried powder samples.

The particles obtained directly after synthesis could easily be stabilized in chloroform by adding oleic acid. In the following, the results of the dynamic light scattering (DLS) measurements of these particles are shown. An average hydrodynamic size based on the volume distribution $x_{V,50}$ between 5 and 7 nm (Fig. 2) is detected, revealing that stabilization of the particles reaching primary particle size is possible. These measured hydrodynamic sizes are in good agreement with the size determined from XRD measurements, as similar values were calculated for the crystallite size. This indicates that each particle consists of a single crystallite which is either surrounded by a fine amorphous layer or by partially reacted precursors or organic compounds from the reaction medium.

The size and morphology of the particles are shown in the TEM images in Fig. 3. The images show a sample of $Mn_{0.6}Zn_{0.4}Fe_2O_4$ particles obtained after 24 h of synthesis. The particles have a size of around 6 nm. Although the particles appear to be spherical at first sight, the high-resolution image shows shamrock-like morphology, with the particles being composed of two or three smaller, aggregated particles.

The measured size from the TEM images is in good agreement with the DLS measurements and the crystallite size calculated *via* the Scherrer equation. This leads to the conclusion that the particles are monocrystalline. To gain an understanding of the particle formation mechanism, samples were taken at different times of reaction during the synthesis of $Mn_{0.6}Zn_{0.4}Fe_2O_4$ particles. The XRD patterns displayed in Fig. 4 show that the reflections strongly increase in intensity with increasing synthesis time from 2 to 24 h. The reflections for the sample drawn after 2 h are very low indicating that the particles are still amorphous. The calculation of the crystallite size from the broadening of the reflections *via* the Scherrer equation shows that the crystallites have a diameter of around 5 nm for all samples apart from the one taken after 2 h where the calculation due to the low signal is not possible.

TEM images of the samples taken after 2 h, 8 h and 14 h of reaction (Fig. 5) show a similar morphology as the samples taken after 24 h. Likewise the samples are largely composed of particles consisting of two or three smaller, aggregated sub-particles. Since after 2 h of synthesis the particles are still amorphous, the resolution of the TEM image is rather poor (Fig. 5a); nonetheless first crystalline particles can be detected. Even at this early stage of synthesis, some of the

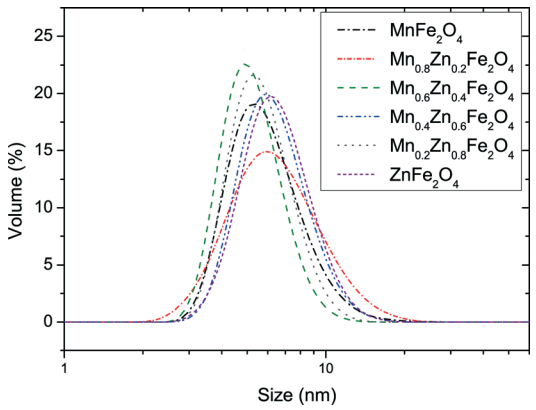

Fig. 2 Dynamic light scattering results for the $Mn_{(1-x)}Zn_xFe_2O_4$ samples dispersed in chloroform.

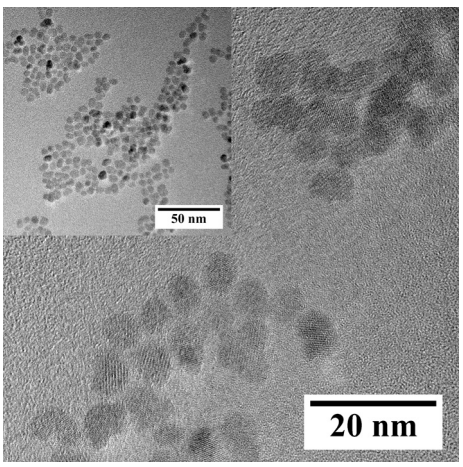

Fig. 3 TEM images of $Mn_{0.6}Zn_{0.4}Fe_2O_4$ nanoparticles after 24 h of synthesis in lower (top left) and higher (bottom) magnification.

 This journal is © The Royal Society of Chemistry 2015

Open Access Article. Published on 04 December 2014. Downloaded on 12/6/2025 6:08:32 AM.
This article is licensed under a Creative Commons Attribution-NonCommercial 3.0 Unported Licence.

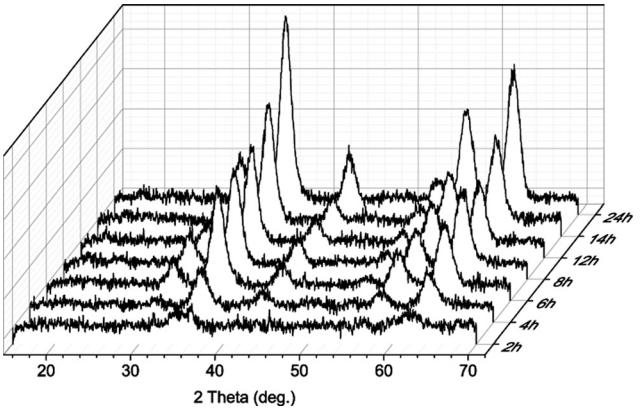

Fig. 4 XRD patterns of the $Mn_{0.6}Zn_{0.4}Fe_2O_4$ samples taken during synthesis.

particles are composed of two or three attached smaller particles. The samples drawn after 8 h (Fig. 5b) and 14 h (Fig. 5c) show crystallized particles. Even though for these samples some single spherical-shaped particles are detected, an increasing fraction of particles are aggregated into the earlier described shamrock-like shape. The aggregates are however single-crystalline, analogous to the particles obtained after 24 h of synthesis.

From the interpretation of the XRD, DLS, and HRTEM data, it is possible to suggest a mechanism of the growth of the particles as is shown schematically in Fig. 6. In the initial stage, spherical and single crystalline particles are formed. In a second step, the particles aggregate with the aggregates showing randomly oriented nanocrystals, originating from the initial single particles. In a third step, the primary

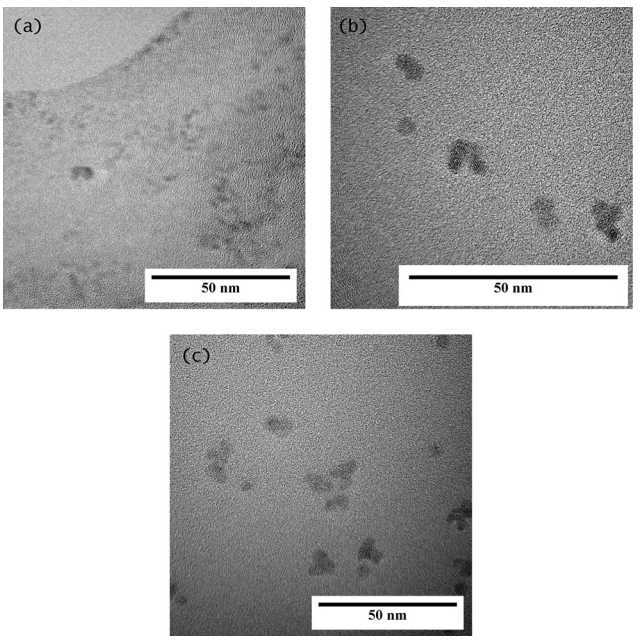

Fig. 5 TEM images of the samples with t_R = 2 h (a), t_R = 8 h (b) and (c) t_R = 14 h.

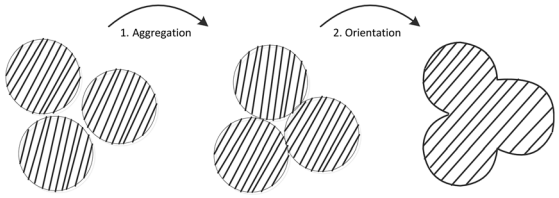

Fig. 6 Schema of the oriented attachment of the nanoparticles.

nanocrystals align along the preferential crystallographic orientation which was identified as the 311 plane from FFT images of a fused nanoparticle (Fig. S5†). This oriented attachment of nanocrystals was monitored *via* TEM analysis for the sample drawn after 14 h and is shown in Fig. 7. In the first image, two crystallites are visible which are already aligned, whilst a third one seen below still shows a different orientation. Due to the exposure to the electron beam of the TEM, the crystals rotate and orientate (middle picture). In the right picture, the fused particle shows one continuous crystallographic orientation. This irreversible alignment of the three particles leads to the described shape of the particles. From the XRD and TEM data obtained for the samples during the synthesis, we can draw the conclusion that this oriented attachment takes place directly after the formation of the particles but continues throughout the whole synthesis, associated with an increase in the fraction of fused particles in the samples over time (Fig. S3†). As two or three particles collide due to Brownian motion, aggregation and oriented attachment takes place at all stages of the synthesis.

Furthermore, small-angle X-ray scattering (SAXS) analysis was carried out for the samples taken during the synthesis to get a deeper insight into the growth mechanism of the particles. The samples were immediately cooled to room temperature after withdrawal to stop any further reaction. Fig. 8 shows the SAXS plots of the dispersions taken after 2 h, 4 h, 12 h and 24 h of synthesis. The scattering intensity I is plotted as a function of the scattering vector on a log–log scale. To extract structural information from SAXS curves of the samples taken after reaction for 2 h and 4 h, the unified equation according to Beaucage[24] was used. The unified approach allows us to calculate a global scattering function (solid lines in Fig. 8) for a particle system consisting of several interrelated structural levels.

As seen in Fig. 8, top, two power law regimes exist in the profile. For scattering vectors $q > 0.8$ nm^{-1}, the slope is −2.4,

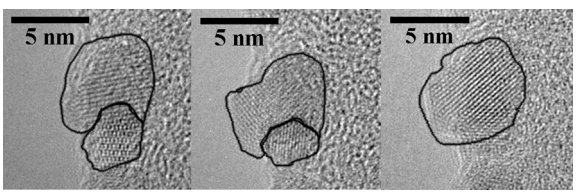

Fig. 7 *In situ* TEM observation of the oriented attachment of $Mn_{0.6}Zn_{0.4}Fe_2O_4$ nanoparticles (image sequence was taken with approximately 2.5 min between the images; hence, the whole sequence was completed after *ca.* 5 minutes).

Open Access Article. Published on 04 December 2014. Downloaded on 12/6/2025 6:08:32 AM.
This article is licensed under a Creative Commons Attribution-NonCommercial 3.0 Unported Licence.

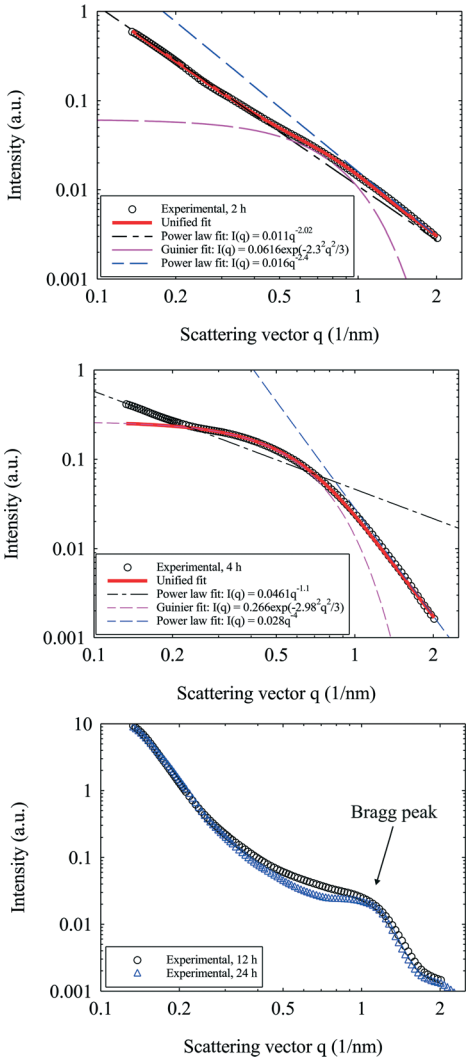

Fig. 8 SAXS patterns of the $Mn_{0.6}Zn_{0.4}Fe_2O_4$ samples taken after 2 h (top), 4 h (center), 12 h and 24 h (bottom) of the synthesis.

indicating that the primary particles have a fractal appearance with a gyration radius of $R_g \approx 2.3$ nm (Guinier fit). In addition, for $q > 0.5$ nm^{-1} the intensity can be described with the approximation $I(q) \sim q^{-2.02}$; this dependency is typically seen for inter-particle scattering. This may result from aggregation of the small particles forming mass fractals with a fractal dimension of ≈2. In Fig. 8, center, the scattering intensity of the particles extracted from the reactor after 4 h is plotted. For the high q regime, also known as the Porod regime, the slope changed to −4, indicating non-fractal surface scattering. Furthermore, a much more pronounced Guinier regime is observed, with a gyration radius for the particles of $R_g \approx 2.98$ nm. Based on these results, the conclusion can be drawn that the particles develop from a small, fractal-like structure to larger and more homogeneous particles, showing non-fractal scaling of the scattering intensity. Moreover, for $q > 0.2$ nm^{-1} the scattering intensity is not constant but shows another power law scaling due to inter-particle scattering. However, only very little data are available for the low q regime and no quantitative interpretation can be extracted from the profile. The sample obtained after 6 h of synthesis shows a similar plot of the scattering intensity as the sample obtained after 4 h. In contrast, the scattering intensity of the dispersions obtained after 12 h of synthesis is clearly changed (Fig. 8, bottom). The profile exhibits a Bragg peak at $q_{peak} \approx 1$ nm^{-1} which corresponds to a regular inter-particle distance (structure factor) of $d_{Bragg} = 2\pi/q_{peak} \approx 6.3$ nm which may be a result of ordered agglomerates (multiplets). For the samples obtained after 24 h, the Bragg peak sharpens to some extent, indicating an increasing ordering of these clusters.

From the SAXS data, the following conclusion can be drawn: Initially the nanoparticles form in an amorphous state with a size of around 2 nm (gyration radius). These ultra-small nanoparticles aggregate, and as the synthesis progresses, these intermediate particles condense due to surface atom diffusion to minimize the surface area and crystallize into defined, crystalline primary particles as supported by XRD measurements (Fig. 4). After 6 h of synthesis, the particles form ordered clusters with an inter-particle distance of 6.3 nm. Throughout the synthesis, the symmetry within these particle clusters increases.

Flame AAS and ICP-OES were employed to determine the Mn/Zn ratio of the six different $Mn_{(1-x)}Zn_xFe_2O_4$ compositions. In Table 1, the measured mol% ratios of zinc and manganese are shown as determined by F-AAS and ICP-OES. The results obtained from the two methods are comparable. It is noted that for each sample the ratio of Mn to Zn differs by about 10% from the expected composition. More Zn^{2+} is incorporated into the particles which is contrary to our expectations, as Mn^{2+} has a higher probability of getting absorbed by a nucleus. The latter cation does not have a preference to occupy one of the crystal sites and gets uniformly distributed among the tetrahedral and the octahedral sites.[25,26] Hence it was expected that more Mn^{2+} is incorporated into the particles. Nonetheless, since the radius of the

Table 1 Composition of synthesized Mn–Zn ferrites, comparing AAS and ICP-OES

	Composition AAS	
Sample	Mn (mol%)	Zn (mol%)
$MnFe_2O_4$	96	4
$Mn_{0.8}Zn_{0.2}Fe_2O_4$	67	33
$Mn_{0.6}Zn_{0.4}Fe_2O_4$	47	52
$Mn_{0.4}Zn_{0.6}Fe_2O_4$	30	70
$Mn_{0.2}Zn_{0.8}Fe_2O_4$	13	87
$ZnFe_2O_4$	1	99
	Composition ICP-OES	
Sample	Mn (mol%)	Zn (mol%)
$MnFe_2O_4$	95	5
$Mn_{0.8}Zn_{0.2}Fe_2O_4$	68	31
$Mn_{0.6}Zn_{0.4}Fe_2O_4$	48	52
$Mn_{0.4}Zn_{0.6}Fe_2O_4$	29	71
$Mn_{0.2}Zn_{0.8}Fe_2O_4$	13	87
$ZnFe_2O_4$	1	99

This journal is © The Royal Society of Chemistry 2015

Open Access Article. Published on 04 December 2014. Downloaded on 12/6/2025 6:08:32 AM.
This article is licensed under a Creative Commons Attribution-NonCommercial 3.0 Unported Licence.

Zn^{2+} cations (0.74 Å) is smaller than that of the Mn^{2+} cation (0.83 Å) it is possible that an increased integration of Mn^{2+} into the lattice leads to an energetically unfavorable distortion of the lattice.

The Curie temperature (T_c) marks the transition temperature from the ferro- or ferrimagnetic to the paramagnetic state. We measured T_c of the calcinated $Mn_{(1-x)}Zn_xFe_2O_4$ samples by TGA. The tendency is that T_c strongly increases with an increasing Mn content, as shown in Fig. 9 (red curve). As expected, the $MnFe_2O_4$ sample has the highest Curie temperature and the sample composed of $ZnFe_2O_4$ has the lowest. Concurrently, the saturation magnetization decreases when the Mn content is decreased and substituted with the non-magnetic ion Zn^{2+} (Fig. 9, black stars).

Spinel ferrites with a cubic crystal structure show two different crystallographic sublattices, composed of tetrahedral (A) and octahedral (B) sites. In the undisturbed case of magnetite Fe_3O_4, the ferrimagnetic structure results from an antiferromagnetic superexchange interaction between the ions on the A and B sites mediated by oxygen ions as well as a ferromagnetic double exchange interaction between the B site ions. In our case, for the $Mn_{(1-x)}Zn_xFe_2O_4$ nanoparticles, the observed tendency of the saturation magnetization can be explained on the basis of the cation distribution, which influences the exchange interaction between the ions at the tetrahedral and octahedral sites. Zn^{2+} ions and Fe^{3+} ions have the preference to occupy the tetrahedral sites. Mn^{2+} and Fe^{2+} do not show this tendency; hence, they are supposed to be equally distributed over all three possible sites.[27,28] As more non-magnetic Zn^{2+} ions occupy the tetrahedral A site, its average magnetic moment decreases and no magnetic interaction between the magnetic ions of the sublattices takes place. Furthermore, due to the presence of Zn ions on the tetrahedral sites the regular distribution of Fe^{2+} and Fe^{3+} on the octahedral sites is distorted.[29] This effect is strengthened by the presence of Mn^{2+} ions on the B sites, whose electron configuration equals that of Fe^{3+} ions. Therefore, the ferromagnetic double exchange interaction between Fe^{2+} and Fe^{3+} ions on the B sites is replaced by an antiferromagnetic superexchange interaction between Fe^{3+} with Fe^{2+} and Mn^{2+}, resulting in a distorted antiferromagnetic structure on the B sites. In conclusion, the disturbed superexchange interaction as well as the canted (non-collinear) spins lead to a decrease in the magnetic moment with increased Zn concentrations. This reduced interaction between the A sites and the B sites results concurrently in a lower value for the Curie temperature.[30] Even though the Curie temperature and the saturation magnetization of the particles are mutually dependent, the saturation magnetization is not the only factor influencing the Curie temperature but for example also the inversion parameter has an impact.[31–33] In addition, surface anisotropy like the formation of a dead layer on the particle surface, existence of random canting of particle surface spins, and non-saturation effects due to broad distribution of particle size or deviation from the normal cation distribution influence the magnetic properties of nanosized particles.[34] In conclusion, even though the general magnetic behavior of the particles can be explained, a full understanding of all observed properties will require further investigations.

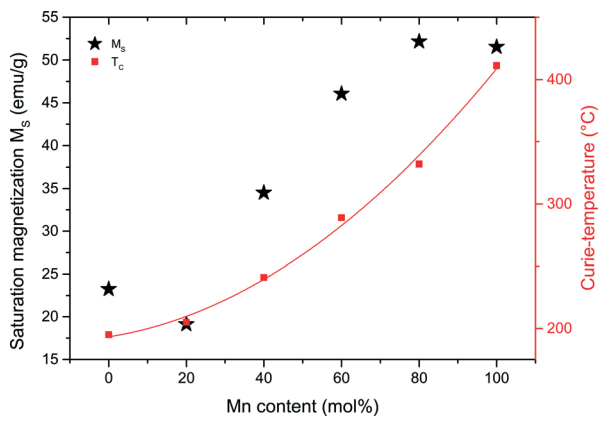

Fig. 9 Specific magnetization and Curie temperature depending on the Mn content.

4. Conclusion

Highly crystalline, ultra-small $Mn_{(1-x)}Zn_xFe_2O_4$ nanoparticles with x between 0 and 1 were obtained in a simple and scalable fashion *via* the non-aqueous sol–gel synthesis. The XRD patterns reveal that the particles have a cubic spinel crystal structure with a crystallite size of around 5 nm.

Through HRTEM, we showed that the nanoparticles have a unique shamrock-type structure, being composed of two or three ≈2 nm sized spherical aggregated particles. The nanoparticles have a size of 6 nm and are monocrystalline. DLS measurements confirmed that the particles have a monodisperse distribution and are highly stable in organic solvents after addition of oleic acid as a surface modifier.

The investigation of the growth mechanism of the particles showed that the nanoparticles grow *via* oriented attachment. We were able to trace the mechanism of oriented attachment described by Penn *et al.*[35] during real-time HRTEM analysis. First the particles were observed to collide forming weakly bound aggregates with randomly attached nanocrystals. In a second step, the particles rearrange forming monocrystalline nanostructures. Right from the start of the synthesis, an oriented attachment of the particles takes place even though the particles are initially formed in a rather amorphous state. Throughout the course of the synthesis, the oriented attachment process continues. After 12 h of synthesis, the primary particles form highly ordered structures with an approximated interparticle distance of 6 nm as shown *via* SAXS analysis.

By variation of the composition of the Mn–Zn ferrites, it is possible to tune the Curie temperature of the particles in a range between 170 °C and 420 °C. We postulated that the saturation magnetization as well as the Curie temperature are influenced by the different distributions of the cations on

Open Access Article. Published on 04 December 2014. Downloaded on 12/6/2025 6:08:32 AM.
This article is licensed under a Creative Commons Attribution-NonCommercial 3.0 Unported Licence.

the A and B sites but that this is not the only factor influencing the magnetic properties of the nanoparticles. Additionally the surface anisotropy or the random canting of spins may contribute to the observed magnetic behavior.

In summary, the presented approach is a simple, efficient, and scalable route to produce ultra-small $Mn_{(1-x)}Zn_xFe_2O_4$ nanoparticles having great potential for various applications particularly in electronics, for electromagnetic heating and biomedicine.

Acknowledgements

The authors thank Prof. G. Goya and A. Ibarra Galián, University of Zaragoza, Spain, for the TEM analysis. Furthermore we thank D. Menzel, Institute of Condensed Matter Physics, TU Braunschweig, for the SQUID measurements, M. Kraken, Institute of Condensed Matter Physics, TU Braunschweig, for the discussion about the magnetic properties and B. Temel for the experimental support throughout the whole project.

References

1 G. Ott, J. Wrba and R. Lucke, *J. Magn. Magn. Mater.*, 2003, **254–255**, 535–537.
2 A. Verma, M. I. Alam, R. Chatterjee, T. C. Goel and R. G. Mendiratta, *J. Magn. Magn. Mater.*, 2006, **300**, 500–505.
3 C. Rath, K. K. Sahu, S. Anand, S. K. Date, N. C. Mishra and R. P. Das, *J. Magn. Magn. Mater.*, 1999, **202**, 77–84.
4 Q. A. Pankhurst, J. Connolly, S. K. Jones and J. Dobson, *J. Phys. D: Appl. Phys.*, 2003, **36**, R167.
5 L. Mei, Z. Dongsheng, H. Junxing, Z. Jia, X. Wei, Y. Hong, Z. Lixin and Y. Jun, *Nanotechnology*, 2013, **24**, 255101.
6 L. Wang, J. Luo, S. Shan, E. Crew, J. Yin, C.-J. Zhong, B. Wallek and S. S. S. Wong, *Anal. Chem.*, 2011, **83**, 8688–8695.
7 A. Hamed, A. G. Fitzgerald, L. Y. Wang, M. Gueorguieva, R. Malik and A. Melzer, *Mater. Technol.*, 2013, **28**, 339–346.
8 V. Zaspalis, V. Tsakaloudi, E. Papazoglou, M. Kolenbrander, R. Guenther and P. V. Valk, *J. Electroceram.*, 2004, **13**, 585–591.
9 J. P. Chen, C. M. Sorensen, K. J. Klabunde, G. C. Hadjipanayis, E. Devlin and A. Kostikas, *Phys. Rev. B: Condens. Matter Mater. Phys.*, 1996, **54**, 9288–9296.
10 J. L. Verhaeghe, G. G. Robbrecht and W. M. Bruynooghe, *Appl. Sci. Res., Sect. B*, 1960, **8**, 128–134.
11 G. Vogler, *Phys. Status Solidi B*, 1971, **43**, K161–K164.
12 R. Arulmurugan, B. Jeyadevan, G. Vaidyanathan and S. Sendhilnathan, *J. Magn. Magn. Mater.*, 2005, **288**, 470–477.
13 J. Moulin, F. Mazaleyrat, Y. Champion, P. Langlois, M. Lecrivain, J. M. Greneche, D. Michel and R. Barrue, *Eur. Phys. J.: Appl. Phys.*, 2003, **23**, 49–54.
14 C. Aubery, C. Solans, S. Prevost, M. Gradzielski and M. Sanchez-Dominguez, *Langmuir*, 2013, **29**, 1779–1789.
15 Y. Y. Meng, Z. W. Liu, H. C. Dai, H. Y. Yu, D. C. Zeng, S. Shukla and R. V. Ramanujan, *Powder Technol.*, 2012, **229**, 270–275.
16 S. Wu, A. Sun, W. Xu, Q. Zhang, F. Zhai, P. Logan and A. A. Volinsky, *J. Magn. Magn. Mater.*, 2012, **324**, 3899–3905.
17 J. Feng, L.-Q. Guo, X. Xu, S.-Y. Qi and M.-L. Zhang, *Phys. B*, 2007, **394**, 100–103.
18 I.-C. Masthoff, F. David, C. Wittmann and G. Garnweitner, *J. Nanopart. Res.*, 2013, **16**, 1–10.
19 C. X. Guo, S. Huang and X. Lu, *Green Chem.*, 2014, **16**, 2571–2579.
20 F. Hu and Y. S. Zhao, *Nanoscale*, 2012, **4**, 6235–6243.
21 Z. Li, P. W. Yi, Q. Sun, H. Lei, H. Li Zhao, Z. H. Zhu, S. C. Smith, M. B. Lan and G. Q. M. Lu, *Adv. Funct. Mater.*, 2012, **22**, 2387–2393.
22 T. A. Cheema and G. Garnweitner, *CrystEngComm*, 2014, **16**, 3366–3375.
23 R. Reske, H. Mistry, F. Behafarid, B. Roldan Cuenya and P. Strasser, *J. Am. Chem. Soc.*, 2014, **136**, 6978–6986.
24 G. Beaucage, *J. Appl. Crystallogr.*, 1995, **28**, 717–728.
25 A. Zapata and G. Herrera, *Ceram. Int.*, 2013, **39**, 7853–7860.
26 R. Gimenes, M. R. Baldissera, M. R. A. da Silva, C. A. da Silveira, D. A. W. Soares, L. A. Perazolli, M. R. da Silva and M. A. Zaghete, *Ceram. Int.*, 2012, **38**, 741–746.
27 C. Rath, S. Anand, R. P. Das, K. K. Sahu, S. D. Kulkarni, S. K. Date and N. C. Mishra, *J. Appl. Phys.*, 2002, **91**, 2211–2215.
28 R. Topkaya, A. Baykal and A. Demir, *J. Nanopart. Res.*, 2012, **15**, 1–18.
29 O. Matthias, *J. Phys. D: Appl. Phys.*, 2012, **45**, 033001.
30 R. Arulmurugan, G. Vaidyanathan, S. Sendhilnathan and B. Jeyadevan, *J. Magn. Magn. Mater.*, 2006, **298**, 83–94.
31 Z. Klencsar, G. Tolnai, L. Korecz, I. Sajo, P. Nemeth, J. Osan, S. Meszaros and E. Kuzmann, *Solid State Sci.*, 2013, **24**, 90–100.
32 D. Vollath, D. V. Szabo, R. D. Taylor and J. O. Willis, *J. Mater. Res.*, 1997, **12**, 2175–2182.
33 M. Hofmann, S. J. Campbell, H. Ehrhardt and R. Feyerherm, *J. Mater. Sci.*, 2004, **39**, 5057–5065.
34 G. Vaidyanathan, R. Arulmurugan, S. D. Likhite, M. R. Anantharaman, M. Vaidya, S. Sendhilnathan and N. D. Senthilram, *Indian J. Eng. Mater. Sci.*, 2004, **11**, 289–294.
35 R. L. Penn and J. F. Banfield, *Science*, 1998, **281**, 969–971.

 This journal is © The Royal Society of Chemistry 2015